Journal of Materials Chemistry A

Dopant arrangements in Y-doped $BaZrO_3$ under processing conditions and their impact on proton conduction: a large-scale first-principles thermodynamics study

Journal:	*Journal of Materials Chemistry A*
Manuscript ID	TA-ART-02-2020-001741.R1
Article Type:	Paper
Date Submitted by the Author:	13-May-2020
Complete List of Authors:	Kasamatsu, Shusuke; Yamagata University - Kojirakawa Campus Osamu, Sugino ; The University of Tokyo Ogawa, Takafumi; Japan Fine Ceramics Center, Nanostructures Research Laboratory Kuwabara, Akihide; Japan Fine Ceramics Center, Nanostructures Research Laboratory

Journal Name

ARTICLE TYPE

Cite this: DOI: 00.0000/xxxxxxxxxx

Dopant arrangements in Y-doped $BaZrO_3$ under processing conditions and their impact on proton conduction: a large-scale first-principles thermodynamics study

Shusuke Kasamatsu,*[a] Osamu Sugino,[b] Takafumi Ogawa,[c] and Akihide Kuwabara[c]

Received Date
Accepted Date

DOI: 00.0000/xxxxxxxxxx

Y-doped $BaZrO_3$ is an ion conductor under intense research for application in medium temperature solid oxide fuel cells. The conductivity is maximized at ∼20% doping, and the decrease with further doping has often been attributed to the association effect, or the trapping of ionic charge carriers by the dopant. This seems like a reasonable conjecture since the dopant and carrier are charged in opposite polarities and should attract each other. However, at such high doping concentrations, many-body interactions between nearby dopants and carriers are likely to modify such a simple two-body attraction picture. Thus, in this work, we employ a large-scale first-principles thermodynamic sampling scheme to directly examine the configuration of dopants and charge-compensating defects at realistic doping concentrations under processing conditions. We find that although there is, indeed, a clear $Y'_{Zr} - V^{\bullet\bullet}_{O}$ association effect at all doping concentrations examined, the magnitude of the effect actually decreases with increasing dopant concentration. We also find that Y'_{Zr}–Y'_{Zr} and $V^{\bullet\bullet}_{O}$–$V^{\bullet\bullet}_{O}$ interactions cannot simply be understood in terms of two-body Coulomb attraction and repulsion, highlighting the importance of many-body effects in understanding the defect chemistry in heavily doped oxides. Finally, we examine the dopant configurations and successfully explain the conductivity maximum based on a percolation vs. many-body trapping picture that has gained attention recently.

1 Introduction

Development of stable and highly conductive solid electrolytes is one of the main goals in the field of solid state ionics, and it is also a key issue for the realization of next-generation solid-state electrochemical devices[1,2]. Typical ceramic-based electrolytes are prepared by substitutional doping of aliovalent ions into insulating oxides. This induces charged ionic defects to satisfy charge neutrality, and if those defects are mobile, they can act as charge carriers. It has been found, however, that the conductivity will usually start to decline with increased doping at far below the maximum doping possible[3]. Understanding of the microscopic mechanism for such decline should lead to design principles for good ionic conductors and has been a topic of intense research for decades.

With the above in mind, we focus, in this work, on the proton-conducting perovskite material Y-doped $BaZrO_3$ (BZY). Acceptor-doped perovskite oxides have been under intense research for application in medium-temperature proton ceramic fuel cells and electrolyzers[4–6], and BZY is known to be one of the most promising due to high proton conductivity and chemical stability. In BZY, the Y dopant is known to almost exclusively occupy the Zr site except in Ba-deficient samples[7,8], so the defect reaction can basically be described using Kröger-Vink notation as follows:

$$2Zr^{\times}_{Zr} + O^{\times}_{O} + Y_2O_3 \rightarrow 2Y'_{Zr} + V^{\bullet\bullet}_{O} + 2ZrO_2. \quad (1)$$

Unfortunately, oxygen vacancies are virtually immobile in this system at temperatures of interest for applications. However, mobile protons can be introduced by a hydration reaction with the oxygen vacancies:

$$H_2O + V^{\bullet\bullet}_{O} + O^{\times}_{O} \rightarrow 2(OH^{\bullet}_{O}). \quad (2)$$

Theoretical and experimental works on BZY and similar accepter-doped perovskite oxides have revealed that the protons thus introduced into the system are covalently bonded with oxygen and

[a] Academic Assembly (Faculty of Science), Yamagata University, 1-4-12 Kojirakawa, Yamagata-shi, Yamagata 990-8560 JAPAN. E-mail: kasamatsu@sci.kj.yamagata-u.ac.jp
[b] The Institute for Solid State Physics, the University of Tokyo, 5-1-5 Kashiwanoha, Kashiwa-shi, Chiba, 277-8581, JAPAN.
[c] Nanostructures Research Laboratory, Japan Fine Ceramics Center, 2-4-1 Mutsuno, Atsuta-ku, Nagoya 456-8587 JAPAN.

migrate through a combination of rotation around oxygen and hopping between adjacent oxygen sites[9–13]. With various efforts in process optimization, the conductivity has now reached 10^{-2} S/cm^{-1} at 500 °C[14–18]. However, the transport number of proton conduction starts to decline above 500 °C due to onset of hole conductivity, so further increase in proton conductivity is necessary if the material is to be used as the electrolyte above 500 °C[18]. Clarification of the defect physics and chemistry in this system is expected to help in this regard, and it should also contribute to fundamental understanding of proton conduction in oxides in general[5].

The conductivity of BZY is known to be maximized at $\sim$ 20% Y doping[18,19], and further doping leads to a decrease in the ionic conductivity. Such decline of the conductivity beyond an optimal dopant concentration is observed almost ubiquitously in acceptor-doped perovskites including BZY, and it has often been attributed to the association effect[9,16,20–24]. Because of the simple explanation that the dopant and carrier are charged in opposite polarities and should attract to form association complexes, the association (i.e., trapping) effect seems to be accepted as a rather universal effect, and it is often argued that the effect would become more decisive with increasing doping concentration. Several computational modeling works on BZY and other acceptor-doped perovskites also indicate significant association between the acceptor dopant and oxygen vacancies or protons[10,13,25–32].

On the other hand, at realistic dopant concentrations, interactions with other dopants and carriers nearby may modify this simple two-body attraction picture. Giannici et al. used EXAFS to examine the local environment around the dopant and found evidence for association of Y'_{Zr} and $V_O^{\bullet\bullet}$ at a lower doping concentration in dry BZY (Eq. 1), but not at higher ones[7]. This suggests that the association effect may not necessarily increase with doping. Such a notion has also been suggested in the literature on fluorite-lattice ion conductors[3]. Another idea that is gaining attention recently is that of percolation of dopants. For example, Kim et al. have shown that the doping concentration dependence of hole conductivity in Fe-doped $BaZrO_3$ can be understood by considering the percolation of dopants through the material[33]. Moreover, Toyoura et al., have argued in recent computational works that protons in BZY at realistic doping concentrations would preferentially migrate along a three-dimensional network of dopants, and that the situation is not described accurately by a simple trapping/de-trapping picture[34,35]. They also stress the importance of Y'_{Zr}–Y'_{Zr} correlations (i.e., certain configurations that lead to strong proton trapping) as well as proton-proton repulsion in determining the conductivity. In addition, Draber et al. pointed out in a recent work that certain ordered dopant configurations would enhance the conductivity due to realization of percolation while avoiding trapping configurations[36]. We also note that a similar idea has been proposed for several Li conductors, although in those cases, the focus has been more on the percolation of carriers themselves rather than dopants[37,38]. Summarizing these works, the one-to-one association effect between the carrier and dopant may not be the deciding factor for the conductivity decline at high doping. Rather, the increase in doping should lead to the formation of a long-range network of dopants along which protons can migrate relatively freely. On the other hand, there are certain dopant configurations that lead to strong trapping of protons, and the number of such configurations is expected to increase with doping. Thus, optimization of processing conditions for maximizing the percolation while minimizing trapping would be a natural route to improving the proton conductivity. This is a challenging task, however, as it is very difficult to obtain atomic-scale 3-dimensional images of dopant configurations from experiment. The same can be said from the computational side: due to difficulties in extracting the correct defect-defect interactions at high concentration from first-principles simulations, the configuration of dopants and carriers at realistic thermodynamic conditions are yet to be resolved.

To tackle this problem, we perform, in this work, a large-scale first-principles thermodynamic sampling simulation to characterize the arrangements of dopants and defects as functions of temperature and dopant content. We employ the replica exchange Monte Carlo method[39,40] to speed up the sampling beyond the traditional Metropolis algorithm. First-principles relaxations and energy calculations based on density functional theory (DFT) are performed on all trial configurations that appear during the Monte Carlo steps; we stress that we do not rely on any model parameterizations. In the near past, such simulations would have been deemed too computationally expensive, but we and some other workers have shown that such an approach has actually become feasible with the combination of parallel algorithms and the advancement of massively parallel supercomputers[41–43].

In this work, we limit our investigation to dry BZY with only oxygen vacancies and Y dopants, although works with other dopants as well as protons may be carried out in the future. This means that we are simulating the powder firing or sintering step which is usually performed in dry air before the introduction of protons through hydration (Eq. (2)). We may assume that the dopant arrangements are fixed in this step because cation mobility is small at lower temperatures employed for further processing (i.e., hydration). In the analysis of the results, we focus on mainly three points:

1. *Defect association and repulsion*—we perform analyses of coordination environments around Y and O vacancies and extract interaction energies among them; although this does not directly correlate with trapping of protons (for that, we need to have protons in the simulation), we can at least provide a picture that may improve our understanding of the association effect in heavily doped ionic conductors in general.

2. *Dopant network formation*—we perform percolation analyses of dopant Y networks to discuss the formation of long-range proton conduction networks as functions of temperature and dopant content.

3. *Proton trapping configurations*—we count the number of proton trapping configurations[34] as functions of temperature and dopant content.

From points 2 and 3, we also discuss the optimal processing conditions for obtaining dopant arrangements that maximizes perco-

lation while minimizing trapping.

We note, in passing, that the current approach only describes the thermodynamics and not the kinetics, so we do not have direct access to, e.g., diffusion constants. However, the dopant arrangements obtained in this work will serve as starting points for kinetic Monte Carlo or master equation calculations of the dynamics of ion diffusion; how the dopant arrangements will affect the correlation effect between successive carrier jumps known to profoundly affect the diffusivity vs. dopant content[35,44] will be of particular interest and may be examined in the near future.

2 Computational methodology

2.1 Computational model

We employ the cubic perovskite unit cell multiplied by 3 in the x, y, and z directions in all of our calculations. This corresponds to 27 Ba, 27 Zr, and 81 O sites with which to perform the configurational sampling. We consider models with 4 different doping concentrations, where 2, 4, 6, and 8 Zr sites are substituted by Y atoms corresponding to 7%, 15%, 22%, and 30% Y doping. We will refer to each of these systems as BZY7, BZY15, BZY22, and BZY30 hereafter. It is noted that the phase behavior in the BaO–ZrO_2–Y_2O_3 system is rather complex, and there is some remaining controversy over the solubility limit of Y in cubic $BaZrO_3$. One group reports full solubility up to $\sim 50\%$[45], while another group reports phase separation into two phases: BZ(I) with low solubility $< 15\%$ and disorder, and BZ(II) with high solubility $> 30\%$ and long-range order[46]. In any case, it seems to be accepted that Y is soluble up to rather high amounts in this system, although the actual attained solubility would depend on various processing conditions.

To simulate firing or sintering in dry air, we only consider the defect reaction in Eq. (1), and assume that 1 oxygen vacancy is introduced in the O sublattice for every 2 Y dopants. The calculation supercell is always charge-neutral, so the charge states of defects are always Y'_{Zr} and $V_O^{\bullet\bullet}$. We do not consider any other charge states, nor any intrinsic defects such as cation vacancies or antisite defects, since their number should be negligible compared to the defects introduced to satisfy charge neutrality as in Eq. (1). As mentioned above, calculations involving protons will be performed in the future. We also neglect the effect of hole polarons which can be introduced through the following defect reaction:

$$\frac{1}{2}O_2 + V_O^{\bullet\bullet} \rightarrow 2h^{\bullet} + O_O^{\times}, \tag{3}$$

as their concentration has been evaluated to be several orders of magnitude smaller than the dopant concentration in a previous theoretical work[47]. Due to their small quantity, we expect that holes will have very little effect on the thermodynamics; we note, however, that the presence of holes does need to be considered when discussing the total conductivity in oxidizing atmosphere[18,48].

We also neglect the phonon contribution to the free energy. Its effect can be significant when the number of atoms change as is the case for vacancy or interstitial formation; this is because the number of vibrational modes will change leading to a rather pronounced impact on the entropy[26,49]. However, the number of atoms of each type is held constant during our simulations according to the preset dopant concentration; thus, we expect that the variations in phonon free energies will be small and have a relatively small impact on the outcome of the Monte Carlo sampling.

Even with these simplifications, the possible number of configurations is huge. For example, the 30% doping model has ${}_{27}C_8$ possible ways to arrange Y atoms on Zr sites and ${}_{81}C_4$ ways to arrange oxygen vacancies on O sites, corresponding to a total of 3 693 627 580 500 configurations. It is not possible to perform calculations on every one of those configurations, and thus we rely on computational statistical physics to sample the most thermodynamically relevant ones.

2.2 Replica exchange Monte Carlo coupled with DFT

Configurational sampling in alloy systems is often performed using Metropolis Monte Carlo sampling based on lightweight models fitted to first-principles calculations. A particular model that has seen much use in the literature is the cluster expansion model, which describes the energetics of lattice systems based on parameterization of local cluster interaction energies[49–54]. However, the cluster expansion model is known to have difficulties in describing complex long-range Coulomb interactions[55], and it is also known that the accuracy degrades for systems with significant lattice relaxation[56]. In addition, constructing the cluster expansion Hamiltonian becomes intractable rather quickly as the number of components increases. Ion conducting oxides often fall in these categories, so we opted to bypass any fitting and sample directly on first-principles energies as we mentioned above.

Obviously, first-principles calculations of meaningful supercell size for disorder sampling are quite costly. That is why many have opted to use cluster expansion in the first place. A naive way to increase the number of samples is to run many calculations in parallel, and this may seem like a good way to take advantage of resources available in present-day supercomputing infrastructures. However, this is actually quite inefficient, since the usual Metropolis algorithm can easily get stuck in local energy minima especially at lower temperatures. The statistical physics community has been dealing with this problem for decades, and we employ one of their most successful ideas: replica exchange, also known as parallel tempering in various contexts[39,40,57].

In the replica exchange method, sampling simulations are performed on several 'replicas', or copies of the system in parallel. Each replica is assigned a different temperature in sequence, and thus replicas with lower temperatures will often get stuck in local minima as mentioned above. To alleviate this problem, the temperatures are swapped between replicas at preset intervals according to a probability based on the Metropolis criterion for the ensemble of replicas:

$$P = \min\{1, \exp[(\beta_i - \beta_j)(E_i - E_j)]\}. \tag{4}$$

Here, i, j are the indices of the replicas, β is the inverse temperature $1/(k_B T)$, and E is the energy of the replica. Essentially, a replica with lower energy will be assigned progressively lower temperatures based on this swapping criterion. This means that

a higher temperature replica, which can move relatively freely in configuration space, will be assigned a lower temperature when it finds a new energy basin. This replica will then be responsible for locating the precise local minimum with simulation at this low temperature. In other words, this scheme allows for each replica to travel between high and low temperatures, providing a good balance between surveillance of the global energy landscape and minima-finding while providing temperature-dependent expectation values at the same time.

In this work, the replica exchange method summarized above is combined with the usual Metropolis Monte Carlo sampling. A Metropolis step consists of randomly choosing either a $Zr_{Zr}^{\times}/Y'_{Zr}$ pair or $V_O^{\bullet\bullet}/O_O^{\times}$ pair, swapping their sites, performing structural relaxation including internal and cell degrees of freedom with DFT, and accepting or rejecting the swap according to the Metropolis probability:

$$P = \min\{1, \exp(-\beta \Delta E)\}, \tag{5}$$

where ΔE is the change in the total energy due to the swap. This Metropolis scheme takes care of the configurational entropy naturally.

The DFT calculations that are performed in the course of the replica exchange Monte Carlo (RXMC) scheme explained above are carried out using VASP code[58], which employs the projector-augmented wave method[59] to describe the electron-ion interactions. The GGA-PBE exchange correlation functional[60] is used throughout this work. The wave functions are expanded using a plane wave basis set with a cutoff energy of 300 eV. The Brillouin zone sampling is carried out only at the Γ point. Relaxation of both the internal coordinates and lattice vectors are performed. During relaxation, changes in the lattice constants lead to denser or sparser calculation meshes compared to the preset energy cutoff. To alleviate this, relaxations are restarted several times where the calculation meshes are reset according to the aforementioned cutoff energy.

The parallel code for performing the replica exchange Monte Carlo steps and managing the direct combination with DFT has been described elsewhere[42], and we have recently released a new version with an improved user interface as open source software at `https://github.com/issp-center-dev/abICS`. We perform two independent calculations for each Y concentration from random starting points using 200 Monte Carlo steps for equilibration and 1400 steps for the calculation of the expectation values for various physical quantities such as coordination numbers. The replica exchange (i.e., swapping of temperatures) is attempted at every step. We employ 16 replicas with temperatures that are separated by equal amounts from 600 K to 2500 K. `pymatgen`[61] is employed heavily for structure handling. The results are shown in subsequent sections with standard deviations calculated from the two independent simulations. That is, the standard deviation of each data point is evaluated as

$$\sigma = \sqrt{(x_1 - \bar{x})^2 + (x_2 - \bar{x})^2}, \tag{6}$$

where x_1 and x_2 are averages calculated from the two independent simulations, respectively, and $\bar{x} = (x_1 + x_2)/2$ is the value presented as the data point. Although a standard deviation value calculated from two samples is questionable as a statistical estimate, it can still serve as an indicator of the convergence of the simulations. We judge the convergence to be acceptable for the discussion presented in subsequent sections, although possibilities of sampling bias due to random initialization will need to be tested as more efficient algorithms and supercomputers become available in the future.

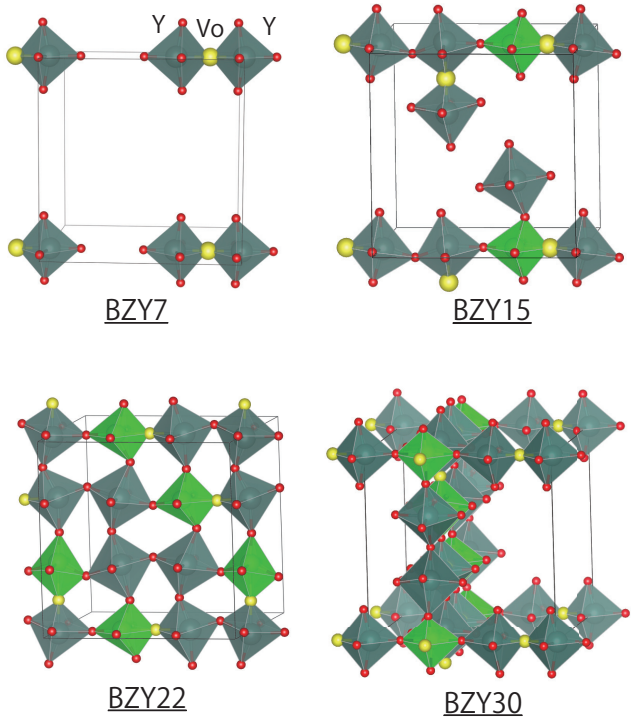

Fig. 1 The lowest-energy configurations that were found in the course of our RXMC simulations for BZY7, BZY15, BZY22, and BZY30. Red, yellow, light green, and dark green spheres correspond to O, O vacancy, Zr, and Y, respectively. Only the (Zr, Y)-O_6 octahedra with at least one defect (Y or O vacancy) is shown.

3 Results and discussion

3.1 Ground-state configurations

Although thermal averages are what actually determine the physical properties of the system, the ground state structures also give us an instructive picture of the important interactions in the system. Figure 1 shows the ground state (or, at least, the lowest energy configurations that were found during the course of our calculations) for varying dopant concentrations. It is clearly seen that at low doping concentration, the Y'_{Zr}–$V_O^{\bullet\bullet}$–Y'_{Zr} complex is most energetically favorable, as would be expected from the Coulombic interactions between charged defects. However, such trend is not as clear at higher concentrations, where many of the $V_O^{\bullet\bullet}$ are coordinated by both Y'_{Zr} and $Zr_{Zr}^{\times}$. This hints at the importance of interactions other than the associative interaction between the dopant and the charge-compensating defect at higher dopant concentrations.

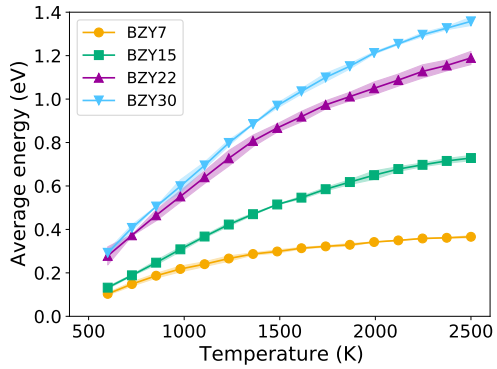

Fig. 2 The calculated average total energy vs. temperature. The zeroes of the energies are taken to be those of the ground state structures reported in Fig. 1. The standard deviation calculated from two independent RXMC runs is shown as colored shadows in this figure and all subsequent figures.

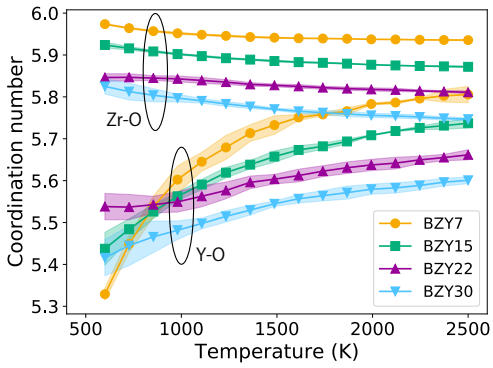

Fig. 3 The calculated average coordination numbers of O around Zr and Y.

We also observe a tendency for the defects (Y'_{Zr} and $V_O^{\bullet\bullet}$) to bunch up in low dimension. In the BZY15 and BZY22 systems, all of the Y ions in the ground state configuration of the $3 \times 3 \times 3$ supercell lie in a single (001) crystallographic plane of the parent cubic lattice. In the BZY30 ground state, all of the Y ions in the supercell lie in two perpendicular planes corresponding to (001) planes. We point out that this behavior may be responsible for the subtle deviation from the perfect cubic lattice reported by some experimental works[7,62]. We do not have a concrete explanation for this behavior, although such localization of defects may be favorable for minimizing elastic strain in the crystal. On a related note, we also observe significant distortion of the octahedra centered on Zr and Y ions in the presence of defects. One clear observation is that Zr and Y that are nearest neighbors to an oxygen vacancy are pushed away, while the O ions are pulled toward the oxygen vacancies. This is easily understood from Coulomb repulsion and attraction. In addition, significant octahedral tilts can also be observed, although it is difficult to figure out a clear pattern for predicting how the octahedra would tilt in the vicinity of defects; we suggest that the distortion patterns are rather long-ranged and cannot be predicted reliably from the local defect structure.

3.2 Temperature dependence of total energy

We start off our examination of temperature-dependent properties by looking at total energies (Fig. 2). The average energy per $3 \times 3 \times 3$ supercell increases with temperature as would be expected (higher temperature allows for less stable configurations). The energies at typical sintering temperatures $\sim$ 1900 K is found to be as high as 1 eV compared to the ground state. This demonstrates clearly that searching for and examining lowest-energy configurations is not enough for these types of situations, as configurational entropy can be quite significant. The slopes, which may be interpreted as the heat capacity in a sense, seem to change continuously; thus we do not detect any clear order-disorder phase transition. We note that the energies presented here do not include any phonon contributions, so we caution against comparing this figure to heat capacities measured in experiment.

3.3 $V_O^{\bullet\bullet}$–Y'_{Zr} association

Next, we examine the association effect by comparing thermal averages of the coordination number of O around Zr and Y atoms (Fig. 3). In the parent perovskite lattice, O ions form a octahedral coordination around Zr leading to a six-fold coordination. Figure 3 shows that the average coordination number is smaller when the central cation is Y in all temperature and doping ranges examined. This means that $V_O^{\bullet\bullet}$ prefers the nearest neighbor site to Y'_{Zr} more than $Zr_{Zr}^{\times}$, clearly indicating the existence of the association effect. The difference between the Zr–O and Y–O coordination numbers decrease as the temperature is increased, which is reasonable considering the more random distribution of defects at elevated temperatures. However, it should be noted that the difference is significant even at above 2000 K, meaning that association exists at all realistic sintering temperatures.

To discuss $V_O^{\bullet\bullet}$–Y'_{Zr} association further, we examine the average first nearest neighbor (1NN) and second nearest neighbor (2NN) coordination numbers of Y'_{Zr} around $V_O^{\bullet\bullet}$ scaled by the number of sites [Fig. 4(a)]. Note that the nearest-neighbor sites discussed here and in subsequent sections are separated by less than half of the supercell length to exclude trivial effects due to supercell periodicity. We find, perhaps surprisingly, that at low temperature, a higher coordination number is obtained for BZY7 compared to higher dopant concentrations. On the other hand, at higher temperatures, the coordination increases monotonously with Y concentration at both 1NN and 2NN sites. However, it should be noted that this does not necessarily reflect the existence of defect association; a higher Y/Zr ratio means a higher coordination number even when the configuration is completely random and no trapping effect exists. Thus, in order to compare the degree of association between different dopant concentrations on an equal footing, we define and calculate the "coordination propensity" as the average coordination number divided by the coordination number when the configuration is completely random [Fig. 4(b)]. A coordination propensity above unity implies attraction and less than unity implies repulsion. We find from the calculated propensities that the association effect does indeed exist, with propen-

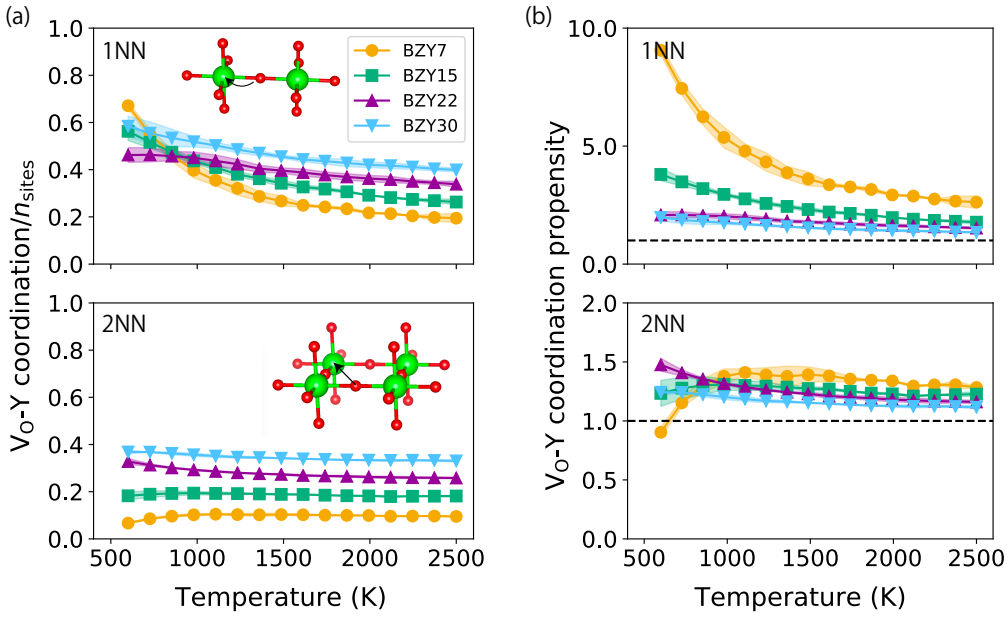

Fig. 4 (a) The calculated average number of Y'_{Zr} at 1NN and 2NN sites to $V^{\bullet\bullet}_O$ scaled by the number of 1NN (2) and 2NN (8) sites. The atomic structure figures in the inset indicate examples of the corresponding NN sites, where O ($O^{\times}_O$ or $V^{\bullet\bullet}_O$) sites are indicated by red spheres and cation ($Zr^{\times}_{Zr}$, Y'_{Zr}) sites by green. (b) The calculated $V^{\bullet\bullet}_O$–Y'_{Zr} coordination propensities (see main text for definition). Horizontal dashed lines are provided at propensities of 1 as guides for the eye.

sities being larger than unity except for the 2NN site at the lowest temperature and lowest dopant concentration examined. We also find that the association effect, especially for the 1NN site, is actually strongest for the lowest concentration and decreases monotonously with increased doping. The decrease seems to saturate around BZY22 to 30.

We can obtain additional insights by examining the number of $V^{\bullet\bullet}_O$ that is coordinated by 0, 1, and 2 Y'_{Zr} [Fig. 5(a)] instead of averaging them out as was done in Fig. 4. We will refer to these three coordination environments as V_O–Zr_2, V_O–ZrY, and V_O–Y_2 hearafter. The basic trend is the same as we found in the preceding analysis: Y'_{Zr} coordination decreases with temperature. A perhaps nontrivial finding from the plot in Fig. 5(a) is that except for the lowest doping concentration and the lowest temperature examined (BZY7 at 500 K), the number of V_O–Y_2 is smaller than V_O–ZrY. Thus, the neutral V_O–Y_2 complex is not the most favorable configuration except at the extremes of low Y content and low temperature. This reinforces the notion discussed above based on the ground state structures with varying Y content. Moreover, these results can be recast in terms of relative free energies assigned to the V_O coordination environments as

$$\Delta F_{D\rightarrow D'} = -k_B T \ln([D']/[D]), \tag{7}$$

where D and D′ are one of V_O–Zr_2, V_O–ZrY, and V_O–Y_2. This equation follows from the often-used definition of free energy vs. an order parameter (in our case, the coordination number of Y'_{Zr}) in terms of the logarithm of relative probabilities[63–65] $\Delta F_{V_O-Zr_2\rightarrow V_O-ZrY}$ may be regarded as the association free energy for coordination by 1 Y and $\Delta F_{V_O-ZrY\rightarrow V_O-Y_2}$ as the association free energy for coordination by an additional Y. The results are plotted in Fig. 5(b), and we find that the results are basically linear vs. temperature. This suggests that the association free energies can be expressed as

$$\Delta F_{D\rightarrow D'} = \Delta E_{assoc} - T\Delta S_{assoc}, \tag{8}$$

where ΔE_{assoc} is interpreted as the temperature-independent association enthalpy (or energy since our calculations are performed at zero pressure) and ΔS_{assoc} as the association entropy. From linear fits of the data in Fig. 5(b), we can obtain the association enthalpies as functions of Y content as shown in Fig. 5(c). We find that the association enthalpy is negative for both the single and double coordination by Y, meaning that the interaction is attractive as expected for defects of opposite polarities. The association is clearly stronger for the second coordination below 20% Y while it becomes comparable for higher Y content. This means that lower Y content favors double Y'_{Zr} coordination around $V^{\bullet\bullet}_O$ while higher Y content favors single Y'_{Zr} coordination. The magnitude of the association energies decreases with Y content in agreement with the coordination propensities presented earlier. It should be noted that the association enthalpies presented here are, in a sense, thermally averaged quantities over all possible configurations in the material and should not be interpreted as the binding energy between isolated defects. This may be why our calculated values are smaller in magnitude than the binding energy between Y'_{Zr} and $V^{\bullet\bullet}_O$ of −0.45 eV reported earlier[26].

3.4 $V^{\bullet\bullet}_O$–$V^{\bullet\bullet}_O$ and Y'_{Zr}–Y'_{Zr} interactions

The weakening of the association effect with increased doping suggests that there are interactions other than Y'_{Zr}–$V^{\bullet\bullet}_O$ attraction that kick in as the Y'_{Zr} and $V^{\bullet\bullet}_O$ concentrations increase. In fact, a similar idea was suggested by a series of kinetic Monte Carlo

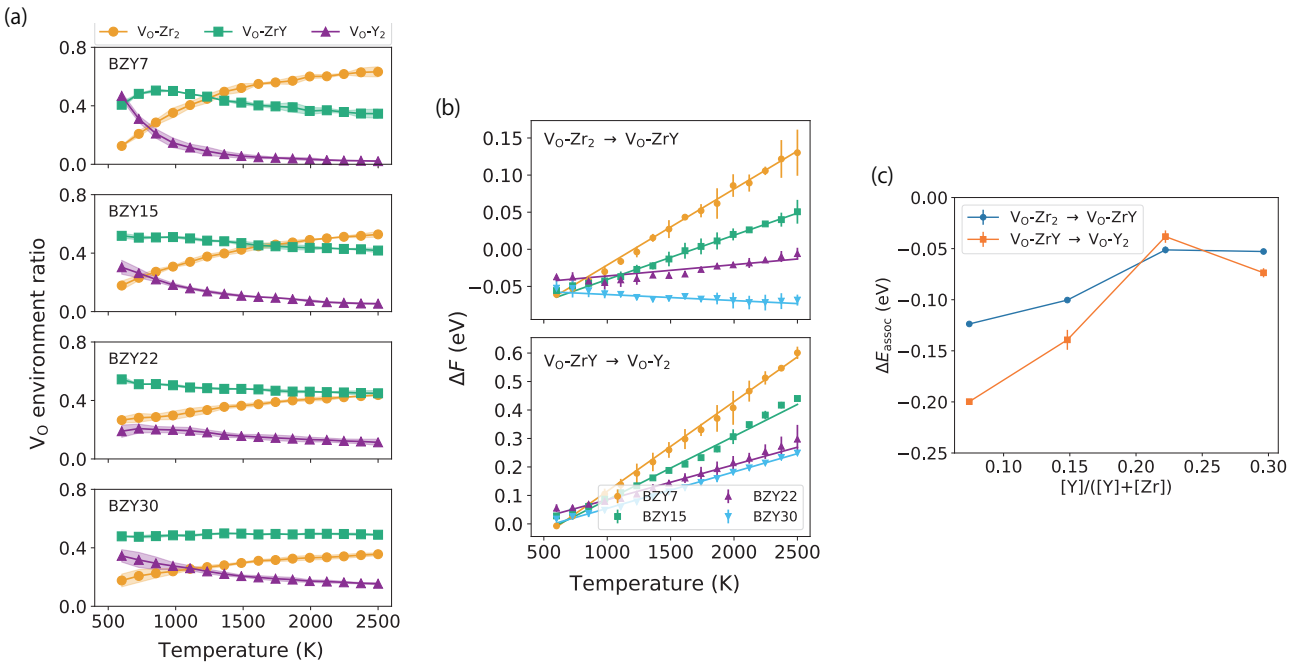

Fig. 5 (a) The ratio of each of the three possible nearest neighbor coordination environments around V_O: V_O–Zr_2 (orange circles), V_O–ZrY (green squares), and V_O–Y_2 (violet triangles) as functions of the temperature. (b) The calculated coordination free energies vs. temperature with a linear fit to the data. (c) The $V_O^{\bullet\bullet}$–Y'_{Zr} association enthalpies for coordination by 1 Y'_{Zr} (blue circles) and coordination by an additional Y'_{Zr} (orange squares) as functions of Y content. The enthalpies are obtained as the y intercept of the linear fitting in (b).

investigations of oxygen ion conduction in ceria by Martin and coworkers[66,67]. To confirm this notion, we repeat the same analysis as above for $V_O^{\bullet\bullet}$–$V_O^{\bullet\bullet}$ and Y'_{Zr}–Y'_{Zr} pairs as shown in Figs. 6–9.

The $V_O^{\bullet\bullet}$–$V_O^{\bullet\bullet}$ coordination increases with Y content as expected from the increased number of $V_O^{\bullet\bullet}$. The coordination propensity (Fig. 6) is found to be quite small up to rather high temperatures at the 1NN site; this may be related not only to Coulomb repulsion, but also to the fact that it is highly unfavorable to have more than one oxygen vacancy at the 1NN site to Zr or Y. The coordination at the 3NN site is also found to be clearly unfavorable, but not as much as the 1NN site at higher temperatures. The $V_O^{\bullet\bullet}$–$V_O^{\bullet\bullet}$ coordination at 2NN and 4NN sites seems to show different behavior depending on the Y content at lower temperatures, although the evaluated error is too large to draw decisive conclusions. At higher temperatures, the coordination propensities at 2NN and 4NN sites quickly converge to unity, which means that the coordination at those sites are virtually random. Examination of the environment ratios for the 1NN $V_O^{\bullet\bullet}$–$V_O^{\bullet\bullet}$ coordination reveals that $V_O^{\bullet\bullet}$ seldom has more than 1 $V_O^{\bullet\bullet}$ at the 1NN sites [Fig. 7(a)]. The corresponding plots of the interaction free energies vs. temperature [Fig. 7(b)] could not be fit well by a single line especially for lower Y content. Thus, we opted to fit the free energies separately for low and high temperatures. The fitted interaction enthalpies [Fig. 7(c)] are positive indicating a repulsive interaction as expected for defects of the same charge polarity. The magnitude of the interaction decreases with increasing Y content, suggesting that screening by other defects (i.e., Y'_{Zr}) reduces the $V_O^{\bullet\bullet}$–$V_O^{\bullet\bullet}$ repulsion. Also, the magnitude decreases with temperature in the cases of BZY15 and BZY22, suggesting that the screening effect increases with temperature. As for BZY30, we see very little temperature dependence compared to BZY15 and BZY22. It should be noted that the above discussion concerns coordination by 1 $V_O^{\bullet\bullet}$. The fact that we seldom see coordination by more than 1 $V_O^{\bullet\bullet}$ means that the repulsion is huge for further coordination regardless of Y content or temperature. We cannot calculate an interaction energy because the probability of having coordination by 2 or more $V_O^{\bullet\bullet}$ is too small and sufficient statistical sampling is not possible within the number of Monte Carlo steps that were carried out.

Next, we turn to the Y'_{Zr}–Y'_{Zr} interaction. Again, the coordination increases with Y content as expected [Fig. 8(a)], and the evaluation of the strength of the interaction requires further analysis. The calculated coordination propensities at 1NN site [Fig. 8(b)] show that at lower temperatures, the pair interaction is clearly attractive for BZY7 and the interaction is very small for BZY15, 22, and 30. Such effective attraction between dopants with same charge polarity may be surprising, but it can be understood as being mediated by the oppositely-charged V_O and is in line with the formation of Y'_{Zr}–$V_O^{\bullet\bullet}$–Y'_{Zr} complexes mentioned earlier. At increased temperature, the 1NN propensity values drop below unity indicating a switching of the interaction from attractive to repulsive with increasing temperature. On the other hand, the 2NN Y'_{Zr}–Y'_{Zr} pairs show a slightly attractive interaction over all temperature ranges except for BZY7 at 600 K. These observations are reinforced by analysis of 1NN Y–Y coordination ratios and the corresponding free energies and enthalpies (Fig. 9).

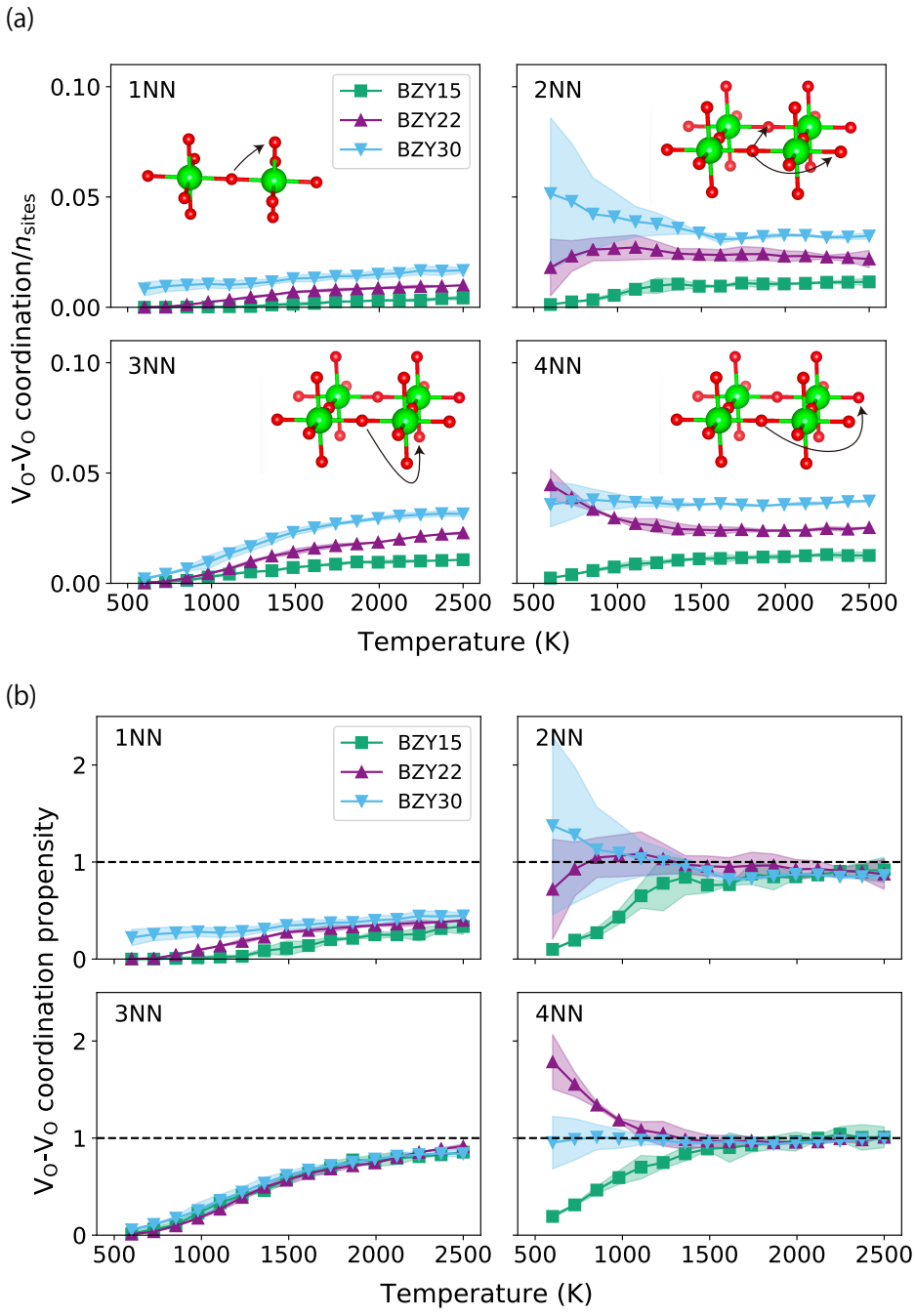

Fig. 6 (a) The calculated average V_O–V_O coordination number for 1NN, 2NN, 3NN, and 4NN sites scaled by the number of 1NN (8), 2NN (6), 3NN (16), and 4NN (12) sites, respectively. The atomic structure figures in the inset indicate examples of the corresponding NN sites, where O (O or V_O) sites are indicated by red spheres and cation ($Zr_{Zr}^{\times}$, Y'_{Zr}) sites by green. (b) The calculated V_O–V_O coordination propensities. It should be noted that no data is provided for BZY7 because there is only one V_O in the calculation cell.

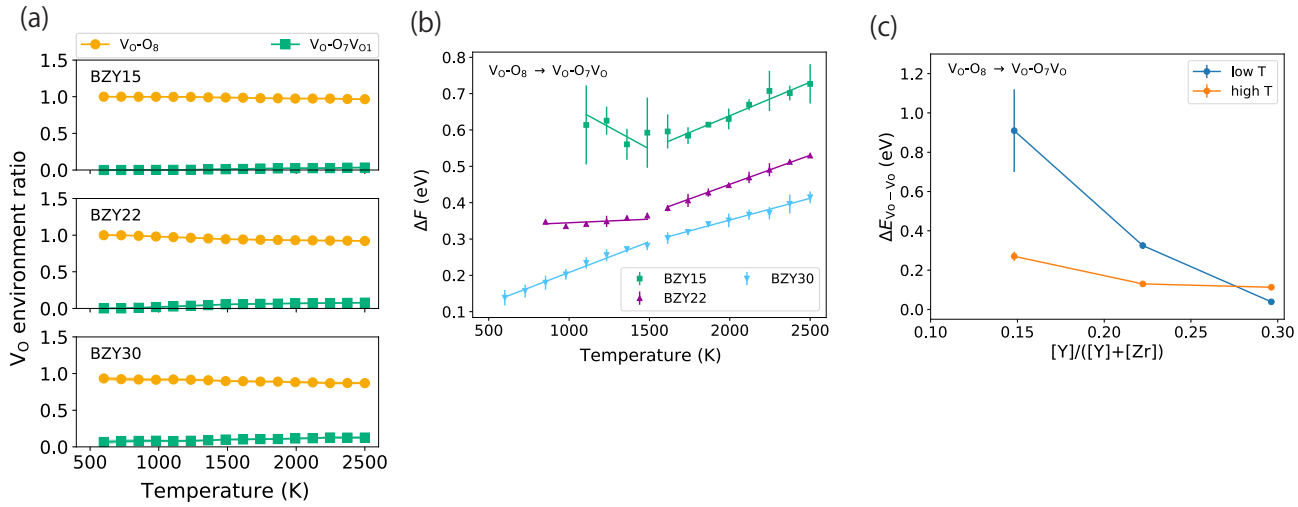

Fig. 7 (a) The ratio of 1NN O site ($O_O^{\times}$ or $V_O^{\bullet\bullet}$) coordination environments around $V_O^{\bullet\bullet}$. Only two cases, coordination by zero $V_O^{\bullet\bullet}$ (orange circles) and coordination by 1 $V_O^{\bullet\bullet}$ (green squares), are shown, as the ratio of coordination by 2 $V_O^{\bullet\bullet}$ was smaller than 0.5% and coordination by 3 $V_O^{\bullet\bullet}$ was never seen in the simulations (coordination by 4 $V_O^{\bullet\bullet}$ or more cannot be observed due to the small number of $V_O^{\bullet\bullet}$ within the limited supercell size). (b) The calculated $V_O^{\bullet\bullet}$–$V_O^{\bullet\bullet}$ interaction free energies with linear fits at temperatures above and below 1500 K. (c) The $V_O^{\bullet\bullet}$–$V_O^{\bullet\bullet}$ interaction enthalpies as functions of Y content. The enthalpies are obtained as the y intercept of the linear fitting in (b).

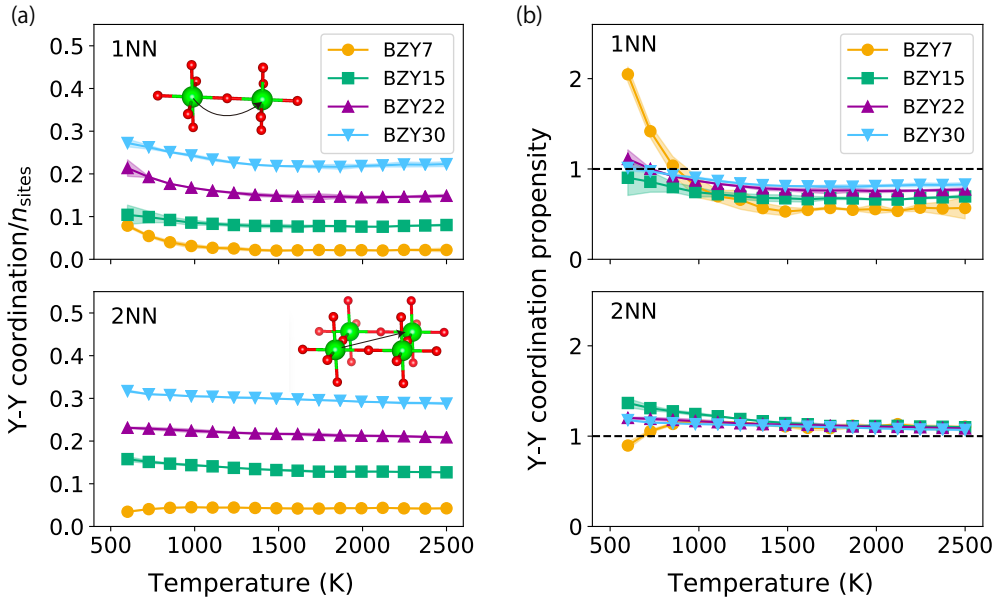

Fig. 8 (a) The calculated average Y'_{Zr}–Y'_{Zr} coordination number at 1NN and 2NN sites scaled by the number of 1NN (6) and 2NN (12) sites. The atomic structure figures in the inset indicate examples of the corresponding NN sites, where O ($O_O^{\times}$ or $V_O^{\bullet\bullet}$) sites are indicated by red spheres and cation ($Zr_{Zr}^{\times}$, Y'_{Zr}) sites by green. (b) The calculated Y'_{Zr}–Y'_{Zr} coordination propensities.

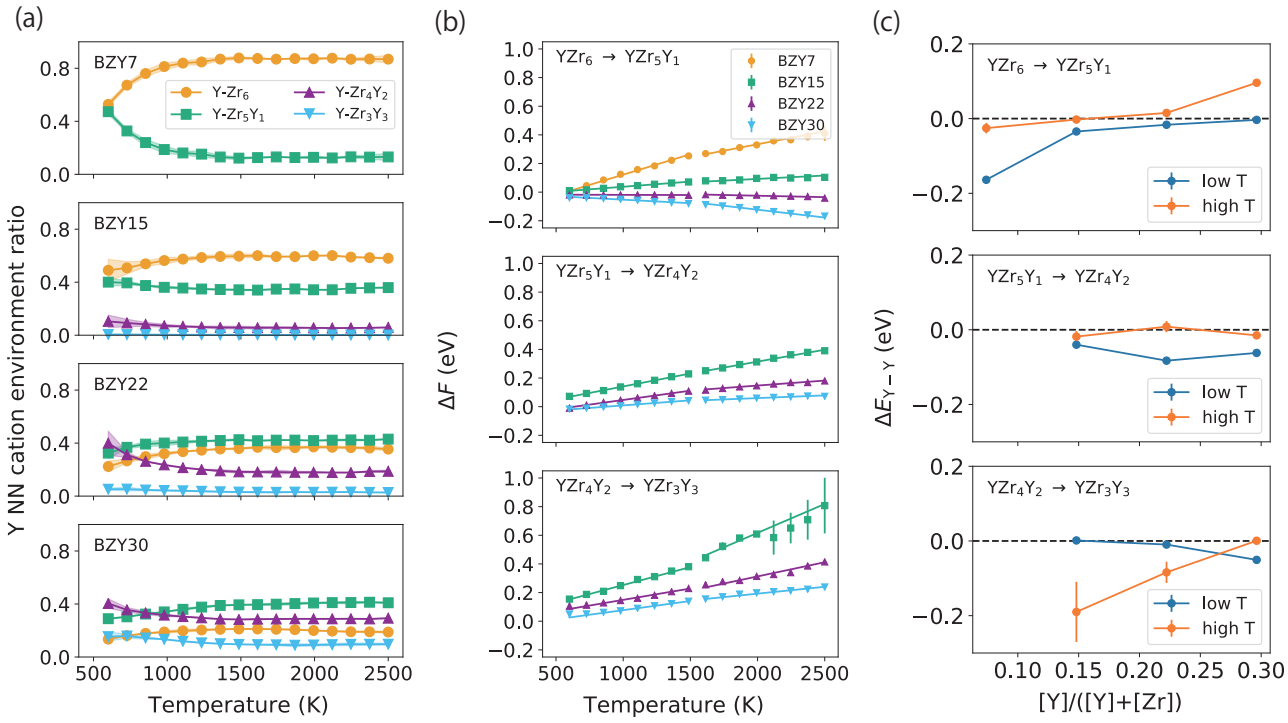

Fig. 9 (a) The ratio of 1NN cation ($Zr_{Zr}^{\times}$ or Y'_{Zr}) coordination environments around Y. Coordination by up to 3 Y'_{Zr} accounted for 98% of all configurations, and coordination by more than 6 Y'_{Zr} was never observed in the simulations. Note that the maximum coordination in our simulation is bound by the number of Y in the calculation cell. (b) The calculated Y'_{Zr}–Y'_{Zr} interaction free energies for first, second, and third coordination by Y'_{Zr} with linear fits at temperatures above and below 1500 K. (c) The Y'_{Zr}–Y'_{Zr} interaction enthalpies as functions of Y content. The enthalpies are obtained as the y intercept of the linear fitting in (b).

The magnitude of the fitted interaction enthalpies are rather small (< 0.1 eV) except for the few cases of (i) ~ -0.2 eV for the first Y'_{Zr} coordination in BZY7 at low temperature and (ii) $\sim +0.1$ eV for the first Y'_{Zr} coordination in BZY30 at high temperature (an interaction of nearly -0.2 eV was also obtained for the third Y'_{Zr} coordination for BZY15 at high tempearature, but the result is questionable due to large predicted error of ± 0.1 eV). Again, this suggests that the Coulomb interactions between the dopants are screened rather well in most cases due to the presence of $V_O^{\bullet\bullet}$. Of the two cases where the interaction was larger, the attraction observed for (i) is due to the formation of Y'_{Zr}–$V_O^{\bullet\bullet}$–Y'_{Zr} complexes at low Y content and low temperature, and repulsion observed for (ii) is most likely due to repulsive interactions starting to kick in at high temperature and high Y content due to the breaking up of Y'_{Zr}–$V_O^{\bullet\bullet}$–Y'_{Zr} complexes.

Since the discussion in preceding sections have been rather complicated, let us summarize here for clarity some of the prominent results on interaction between nearest neighbors:

1. Y'_{Zr}–$V_O^{\bullet\bullet}$ interaction is clearly attractive, although the magnitude of the interaction *decreases with increasing dopant/vacancy content*. This association effect remains even above usual sintering temperatures.

2. $V_O^{\bullet\bullet}$–$V_O^{\bullet\bullet}$ interaction at the 1NN site is strongly repulsive, not only due to Coulomb repulsion but also due to the fact that it is highly unfavorable to have more than one $V_O^{\bullet\bullet}$ coordinating Zr or Y (1NN $V_O^{\bullet\bullet}$s share one nearest neighbor cation).

3. Y'_{Zr}–Y'_{Zr} interaction can switch between repulsive and attractive depending on temperature and dopant concentration. This is most likely due to formation and breaking up of Y'_{Zr}–$V_O^{\bullet\bullet}$–Y'_{Zr} complexes.

Thus, it is clear that the effective interaction between defects cannot be determined simply from arguments based on two-body Coulomb interactions. The interaction between defects with the same charge polarity is not always repulsive, and the magnitude of the interaction is highly dependent on the dopant content and temperature. The behavior also depends on the specific defect; $V_O^{\bullet\bullet}$–$V_O^{\bullet\bullet}$ interaction is always repulsive for 1NN coordination while Y'_{Zr}–Y'_{Zr} interaction can be attractive or repulsive depending on various conditions. The latter may be due to having an O site between 1NN Y'_{Zr}–Y'_{Zr} pairs, or due to the smaller formal charge of -1 for Y'_{Zr} compared to +2 for $V_O^{\bullet\bullet}$.

3.5 Dopant networks and trapping sites

As noted in the introduction, we cannot directly infer the proton conductivity from our results. However, the dopant distribution determined in our work should be directly linked to the conductivity after hydration and introduction of protons (Eq. 2). Toyoura et al. have reported based on kinetic Monte Carlo simulations that protons tend to migrate along a three-dimensional network of dopants[34]. They also suggested that a certain triangular Y'_{Zr} configuration (Fig. 10) shows strong proton trapping and is detrimental to proton conductivity. More recently, they discussed the effect of proton-proton interaction on the conductivity through

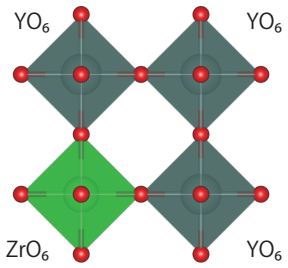

Fig. 10 Triangular configuration of three Y'_{Zr} that was shown to act as trapping sites for protons in Ref. 34.

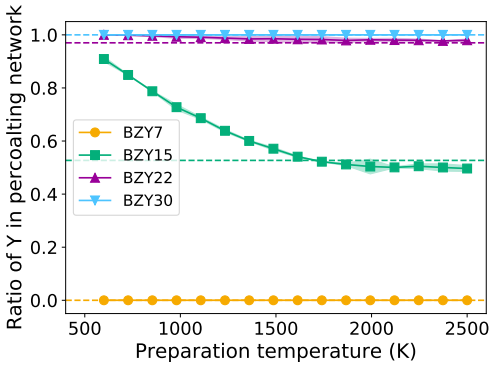

Fig. 11 The ratio of Y ions that participate in a percolating dopant network as functions of temperature and Y content. The horizontal dashed lines correspond to the ratios calculated from 1000 randomly generated configurations for each Y content.

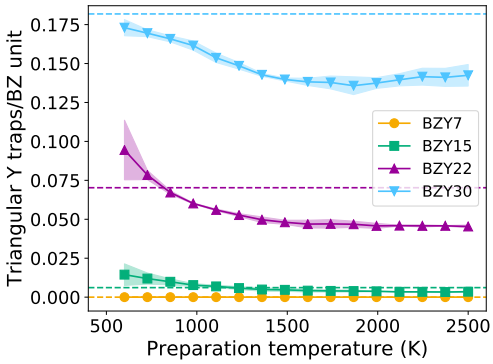

Fig. 12 The number of triangular Y clusters (Fig. 10) comprised of Y that participate in a percolating dopant network as functions of temperature and Y content. The horizontal dashed lines indicate the corresponding quantities calculated by sampling from 1000 randomly generated configurations for each Y content.

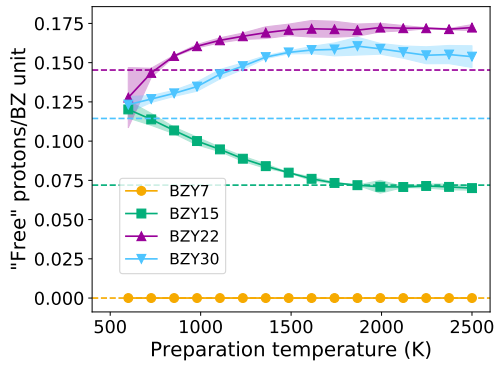

Fig. 13 The number of "free" protons calculated based on assumptions in the main text as functions of temperature and Y content. The horizontal dashed lines correspond to the corresponding quantities calculated by sampling from 1000 randomly generated configurations for each Y content.

an approach based on the master equation for ion diffusion; their results indicate that filling of these trap sites by protons will allow other protons to avoid being trapped, leading to a decrease in the apparent activation energy for diffusion[35]. Motivated by their work, we decided to examine the network formation and the number of trap sites in our calculations as follows.

First, we calculate the number of Y'_{Zr} that participate in a percolating network as shown in Fig. 11. The network is defined by connecting Y'_{Zr} that are within 2NN from each other [Fig. 8(a) inset], since proton hopping paths connect 2NN cation sites (see e.g., Ref. 68). The percolation is detected within the periodic boundary condition by employing a scheme proposed earlier[69,70]. We find that Y'_{Zr} in BZY7 seldom form percolating networks (the number is strictly zero because of the limited unit cell size, but the value is likely to be very small even when employing larger unit cells). On the other hand, more than 95% of Y'_{Zr} in BZY22 or BZY30 take part in forming a percolating network regardless of temperature. The percolation threshold is found to be close to 15% Y; 90% of Y'_{Zr} participate in a percolating network at low temperature due to formation of two-dimensional defect clusters (see Fig. 1) while the value drops to $\sim 50\%$ at elevated temperatures, presumably due to the breaking up of the clusters.

Next, we examine the number of triangular trapping configurations in the percolating network as shown in Fig. 12. Basically, the number increases with Y content as may be expected. An interesting aspect is that the number of trapping configurations decreases with increasing temperature and does not converge to the values sampled from randomly generated configurations within a realistic sintering temperature range. This suggests that simulations based on randomly distributed dopants can lead to an overestimation of trapping.

The preceding analyses can be combined to calculate the concentration of "free" protons based on a few assumptions. Our first assumption is that each Y dopant that is not part of the percolating network traps one proton. The second assumption is that the triangular Y'_{Zr} configuration within the percolating network traps one proton at a time, and that the trapped proton does not block the diffusion of other protons. The third assumption is that the $V_O^{\bullet\bullet}$ are fully hydrated, so one proton exists in the system per Y dopant. This is obviously a simplification, and we note that increasing the degree of hydration is an issue that is under active research[19,24,30–32]; the following results correspond to the ideal case of 100% hydration. The results are plotted in Fig. 13. From comparison of the results for differing Y content, we find that the number of free protons is maximized for BZY22 and drops with further increase in Y content in agreement with the conductivity maximum observed in experiment. This suggests that the concentration of "free" protons as defined according to the above assumptions is a good descriptor for the observed conductivity, and that the conductivity maximum is due to the competition between percolating network formation and the increase in trap sites within the percolating network. Turning our attention to the temperature dependence, we find that the number of free protons decreases with temperature for BZY15. This is because the percolating network will break up as temperature is increased (Fig. 11). This may be a potential explanation for the decrease in conductivity after sintering for extended periods that is observed only around this dopant content[18]. For higher dopant concentrations, BZY22 and BZY30, the number of free protons increases with temperature up to about 1900 K, which is close to the typical sintering temperature used for this material[18]. The increase can be explained by the fact that the network connectivity does not depend very much on temperature while the number of trap sites clearly decreases with temperature (Fig. 12). This suggests that the bulk conductivity for higher Y content will improve with sintering at higher temperatures. The final result is that the optimal dopant content is around BZY22 and sintering should be performed at as high a temperature as possible, in agreement with experimental works that report the best conductivities[15,18].

4 Conclusions

In this work, we performed a large-scale first-principles thermodynamic sampling of defect (Y'_{Zr} and $V_O^{\bullet\bullet}$) configurations in Y-doped $BaZrO_3$. We find that although the association effect between the dopant Y and charge-compensating $V_O^{\bullet\bullet}$ prevails at lower dopant concentrations as suggested by previous theoretical works, the situation becomes much more complicated as the dopant content increases to levels that are known to be optimal for ionic conductivity. Especially, we find that the magnitude of the association enthalpy decreases with increasing Y content; we attribute this to various many-body effects in the system such as $V_O^{\bullet\bullet}$–$V_O^{\bullet\bullet}$ repulsion and screening by other defects in the system. From this, we point out that one should be careful in assuming that simple one-to-one defect association is responsible for conductivity decline at high dopant content. Instead, the optimal dopant concentration and processing temperature in experiment is reproduced almost quantitatively by considering the competition between the formation of a percolating dopant network and formation of certain trapping configurations. An important and general take-away message from this work is that dopant arrangements are far from random in heavily doped oxides, even after sintering, and even if the morphology looks to be uniform. Thus, taking processing condition-dependent dopant arrangements into account as we have done is imperative for quantitative simula-

tions; it should also provide a route to theory-lead optimization of materials selection, dopant concentration, and processing conditions for various materials properties in heavily doped oxides.

Conflicts of interest

There are no conflicts to declare.

Acknowledgements

The calculations were performed on the joint-use supercomputer system at Institute for Solid State Physics, the University of Tokyo. This research was supported by the Ministry of Education, Culture, Sports, Science and Technology through "Priority Issue on Post-K computer" (Development of new fundamental technologies for high-efficiency energy creation, conversion/storage and use) and by CREST, Japan Science and Technology Agency Grant Number JPMJCR18J2. S. K. is also supported by Grant-in-Aid for Young Scientists (No. 19K15287) by Japan Society for the Promotion of Science. Atomic structure figures were created using the visualization software VESTA[71].

Notes and references

1 K. Funke, *Sci. Technol. Adv. Mater.*, 2013, **14**, 043502.
2 O. Yamamoto, *Sci. Technol. Adv. Mater.*, 2017, **18**, 504–527.
3 J. A. Kilner, *Solid State Ionics*, 2000, **129**, 13–23.
4 H. Iwahara, T. Esaka, H. Uchida and N. Maeda, *Solid State Ionics*, 1981, **3/4**, 359–363.
5 T. Norby, *Solid State Ionics*, 1999, **125**, 1–11.
6 K. D. Kreuer, *Annu. Rev. Mater. Res*, 2003, **33**, 333–359.
7 F. Giannici, M. Shirpour, A. Longo, A. Martorana, R. Merkle and J. Maier, *Chem. Mater.*, 2011, **23**, 2994–3002.
8 D. Han, K. Kishida, K. Shinoda, H. Inui and T. Uda, *J. Mater. Chem. A*, 2013, **1**, 3027–3033.
9 K. D. Kreuer, *Solid State Ionics*, 1999, **125**, 285–302.
10 M. S. Islam, R. A. Davies and J. D. Gale, *Chem. Mater.*, 2001, **13**, 2049–2055.
11 P. G. Sundell, M. E. Björketun and G. Wahnström, *Phys. Rev. B*, 2007, **76**, 094301.
12 Q. Zhang, G. Wahnström, M. E. Björketun, S. Gao and E. Wang, *Phys. Rev. Lett.*, 2008, **101**, 215902.
13 P. Raiteri, J. D. Gale and G. Bussi, *J. Phys. Condens. Matter*, 2011, **23**, 334213.
14 Y. Yamazaki, R. Hernandez-Sanchez and S. M. Haile, *Chem. Mater.*, 2009, **21**, 2755–2762.
15 Y. Yamazaki, R. Hernandez-Sanchez and S. M. Haile, *J. Mater. Chem.*, 2010, **20**, 8158.
16 Y. Yamazaki, F. Blanc, Y. Okuyama, L. Buannic, J. C. Lucio-Vega, C. P. Grey and S. M. Haile, *Nat. Mater.*, 2013, **12**, 647–651.
17 L. Bi and E. Traversa, *J. Mater. Res.*, 2014, **29**, 1–15.
18 D. Han and T. Uda, *J. Mater. Chem. A*, 2018, **6**, 18571–18582.
19 D. Han, N. Hatada, T. Uda and R. Koc, *J. Am. Ceram. Soc.*, 2016, **99**, 3745–3753.
20 R. Hempelmann, M. Soetratmo, O. Hartmann and R. Wäppling, *Solid State Ionics*, 1998, **107**, 269–280.
21 R. Merkle and J. Maier, *Phys. Chem. Chem. Phys.*, 2003, **5**, 2297–2303.
22 E. Fabbri, D. Pergolesi, S. Licoccia and E. Traversa, *Solid State Ionics*, 2010, **181**, 1043–1051.
23 M. D. Gonçalves, P. S. Maram, R. Muccillo and A. Navrotsky, *J. Mater. Chem. A*, 2014, **2**, 17840–17847.
24 I. Oikawa and H. Takamura, *Chem. Mater.*, 2015, **27**, 6660–6667.
25 G. C. Mather and M. Saiful Islam, *Chem. Mater.*, 2005, **17**, 1736–1744.
26 P. G. Sundell, M. E. Björketun and G. Wahnström, *Phys. Rev. B*, 2006, **73**, 104112.
27 R. A. Davies, M. S. Islam and J. D. Gale, *Solid State Ionics*, 1999, **126**, 323–335.
28 M. S. Islam, *J. Mater. Chem.*, 2000, **10**, 1027–1038.
29 M. S. Islam, P. R. Slater, J. R. Tolchard and T. Dinges, *Dalt. Trans.*, 2004, **3**, 3061–3066.
30 J. A. Dawson, J. A. Miller and I. Tanaka, *Chem. Mater.*, 2015, **27**, 901–908.
31 H. Takahashi, I. Yashima, K. Amezawa, K. Eguchi, H. Matsumoto, H. Takamura and S. Yamaguchi, *Chem. Mater.*, 2017, **29**, 1518–1526.
32 H. Takahashi, I. Oikawa and H. Takamura, *J. Phys. Chem. C*, 2018, **122**, 6501–6507.
33 D. Kim, S. Miyoshi, T. Tsuchiya and S. Yamaguchi, *Solid State Ionics*, 2014, **262**, 875–878.
34 K. Toyoura, W. Meng, D. Han and T. Uda, *J. Mater. Chem. A*, 2018, **6**, 22721–22730.
35 K. Toyoura, T. Fujii, N. Hatada, D. Han and T. Uda, *J. Phys. Chem. C*, 2019, **123**, 26823–26830.
36 F. M. Draber, C. Ader, J. P. Arnold, S. Eisele, S. Grieshammer, S. Yamaguchi and M. Martin, *Nature Mater.*, 2019.
37 Y. Inaguma and M. Itoh, *Solid State Ionics*, 1996, **86-88**, 257–260.
38 H. Ji, A. Urban, D. A. Kitchaev, D.-H. Kwon, N. Artrith, C. Ophus, W. Huang, Z. Cai, T. Shi, J. C. Kim, H. Kim and G. Ceder, *Nature Commun.*, 2019, **10**, 592.
39 R. Swendsen and J. Wang, *Phys. Rev. Lett.*, 1986, **57**, 2607–2609.
40 K. Hukushima and K. Nemoto, *J. Phys. Soc. Jpn.*, 1996, **65**, 1604–1608.
41 S. N. Khan and M. Eisenbach, *Phys. Rev. B*, 2016, **93**, 024203.
42 S. Kasamatsu and O. Sugino, *J. Phys.: Condens. Matter*, 2019, **31**, 085901.
43 R. B. Wexler, T. Qiu and A. M. Rappe, *J. Phys. Chem. C*, 2019, **123**, 2321–2328.
44 R. Krishnamurthy, Y.-G. Yoon, D. J. Srolovitz and R. Car, *J. Amer. Ceram. Soc.*, 2004, **87**, 1821–1830.
45 S. Imashuku, T. Uda, Y. Nose and Y. Awakura, *J. Phase Equilib. Diffus.*, 2010, **31**, 348–356.
46 Y. Oyama, A. Kojima, X. Li, R. B. Cervera, K. Tanaka and S. Yamaguchi, *Solid State Ionics*, 2011, **197**, 1–12.
47 A. Lindman, P. Erhart and G. Wahnström, *Phys. Rev. B*, 2015, **91**, 245114.

48 A. Lindman, P. Erhart and G. Wahnström, *Phys. Rev. B*, 2016, **94**, 075204.

49 C. B. Gopal and A. van de Walle, *Phys. Rev. B*, 2012, **86**, 134117.

50 J. M. Sanchez, F. Ducastelle and D. Gratias, *Physica A*, 1984, **128A**, 334–350.

51 A. van de Walle, M. Asta and G. Ceder, *Calphad*, 2002, **26**, 539 – 553.

52 A. Seko, Y. Koyama and I. Tanaka, *Phys. Rev. B*, 2009, **80**, 165122.

53 J. M. Sanchez, *J. Phase Equilib. Diffus.*, 2017, **38**, 238–251.

54 Q. Wu, B. He, T. Song, J. Gao and S. Shi, *Comput. Mater. Sci.*, 2016, **125**, 243–254.

55 A. Seko and I. Tanaka, *J. Phys.: Condens. Matter*, 2014, **26**, 115403.

56 A. H. Nguyen, C. W. Rosenbrock, C. S. Reese and G. L. Hart, *Phys. Rev. B*, 2017, **96**, 014107.

57 D. J. Earl and M. W. Deem, *Phys. Chem. Chem. Phys.*, 2005, **7**, 3910–3916.

58 G. Kresse and J. Furthmüller, *Phys. Rev. B*, 1996, **54**, 11169–11186.

59 P. E. Blöchl, *Phys. Rev. B*, 1994, **50**, 17953–17979.

60 J. P. Perdew, K. Burke and M. Ernzerhof, *Phys. Rev. Lett.*, 1996, **77**, 3865–3868.

61 S. P. Ong, W. D. Richards, A. Jain, G. Hautier, M. Kocher, S. Cholia, D. Gunter, V. L. Chevrier, K. A. Persson and G. Ceder, *Comput. Mater. Sci.*, 2013, **68**, 314–319.

62 K. D. Kreuer, S. Adams, W. Münch, A. Fuchs, U. Klock and J. Maier, *Solid State Ionics*, 2001, **145**, 295–306.

63 M. Bonomi, D. Branduardi, G. Bussi, C. Camilloni, D. Provasi, P. Raiteri, D. Donadio, F. Marinelli, F. Pietrucci, R. A. Broglia and M. Parrinello, *Comput. Phys. Commun.*, 2009, **180**, 1961–1972.

64 C. Hartmann, J. C. Latorre and G. Ciccotti, *Eur. Phys. J. Spec. Top.*, 2011, **200**, 73–89.

65 D. Frenkel and B. Smit, *Understanding Molecular Simulation: From Algorithms to Applications*, Academic Press, San Diego, 2nd edn., 2002, vol. 1.

66 B. O. H. Grope, T. Zacherle, M. Nakayama and M. Martin, *Solid State Ionics*, 2012, **225**, 476–483.

67 J. Koettgen, S. Grieshammer, P. Hein, B. O. H. Grope, M. Nakayama and M. Martin, *Phys. Chem. Chem. Phys.*, 2018, **20**, 14291–14321.

68 K. Toyoura, D. Hirano, A. Seko, M. Shiga, A. Kuwabara, M. Karasuyama, K. Shitara and I. Takeuchi, *Phys. Rev. B*, 2016, **93**, 054112.

69 J. Machta, Y. S. Choi, A. Lucke, T. Schweizer and L. M. Chayes, *Phys. Rev. E*, 1996, **54**, 1332–1345.

70 M. E. J. Newman and R. M. Ziff, *Phys. Rev. E*, 2001, **64**, 016706.

71 K. Momma and F. Izumi, *J. Appl. Crystallogr.*, 2008, **41**, 653.

The proton conductivity maximum in doped $BaZrO_3$ is explained by a percolation vs. many-body trapping picture using first-principles thermodynamics calculations.